# Morphology and line tension of twist disclinations in a nematic liquid crystal

# (Electronic Supplementary Information)

Yihao Chen[a], Mina Mandić[b], Charlotte G. Slaughter[a], Michio Tanaka[a], James M. Kikkawa[a], Peter J. Collings[a,b], and A. G. Yodh[a]

[a] Department of Physics and Astronomy, University of Pennsylvania, Philadelphia, PA, U.S.A.
[b] Department of Physics & Astronomy, Swarthmore College, Swarthmore, PA, U.S.A.

## Contents

# 1 Minimization of the total line energy and numerical method

The total energy of the real disclination is obtained from an integral along the disclination contour, which depends on depth, *i.e.*,

$$
\begin{aligned}
F_{\text{line total}} &= \int_0^l f_l(s)ds \\
&= \int_{-\frac{M}{2}}^{\frac{M}{2}} f_l(z(\xi))\sqrt{1+z'^2}d\xi,
\end{aligned}
\tag{S.1}
$$

where $l$ is the total length of the disclination between the two pinned ends, $s$ is the length along the disclination contour, $z(\xi)$ is the bending shape (depth) of the disclination with the $\xi$-axis running through and centered between two pinned ends.

Minimization of $F_{\text{line total}}$ based on variational calculus yields

$$
\begin{aligned}
-\frac{d}{d\xi}\frac{\partial[f_l(z(\xi))\sqrt{1+z(\xi)'^2}]}{\partial z(\xi)'} + \frac{\partial[f_l(z(\xi))\sqrt{1+z(\xi)'^2}]}{\partial z(\xi)} &= 0 \\
-\frac{d}{d\xi}[f_l(z(\xi))\frac{z(\xi)'}{\sqrt{1+z(\xi)'^2}}] + \frac{df_l(z(\xi))}{dz(\xi)}\sqrt{1+z(\xi)'^2} &= 0 \\
-\frac{df_l(z(\xi))}{dz(\xi)}\frac{z(\xi)'^2}{\sqrt{1+z(\xi)'^2}} - f_l(z(\xi))\frac{z(\xi)''}{[1+z(\xi)'^2]^{3/2}} + \frac{df_l(z(\xi))}{dz(\xi)}\sqrt{1+z(\xi)'^2} &= 0 \\
-f_l(z(\xi))z(\xi)'' + \frac{df_l(z(\xi))}{dz(\xi)}[1+z(\xi)'^2] &= 0 \\
z(\xi)'' = \frac{1}{f_l(z(\xi))}\frac{df_l(z(\xi))}{dz(\xi)}[z(\xi)'^2+1]. &
\end{aligned}
\tag{S.2}
$$

The last row is Eq. (2) of the main text. We solve it using the solve_bvp function from the scipy module of python, which solves boundary value problems of differential equations.

In the main text we focus primarily on the solutions for disclinations with two ends pinned on the *same* substrate. Here, Figure S1 shows the shape of the disclination with two ends pinned on *different* substrates from the numerical solution of Eq. (2) of the main text for various values of $D_c$ and $M$.

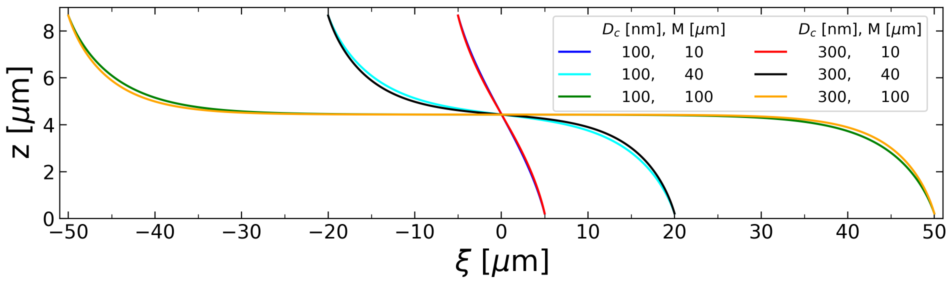


Figure S1: Profiles of disclinations with ends pinned on different substrates predicted by Eq. (2) of the main text with various $D_c$ and $M$ values as indicated by the legends.

# 2 Model for energy balance

Figure S2 shows a schematic plot of a free disclination bending in a magnetic field. The bold blue line is the free disclination at zero magnetic field; the thin blue line is the surface disclination, and the black line is the bending disclination due to the magnetic field. $R$ is the radius of the circle fit to the bent free disclination, $l$ is the length of the free disclination, $M$ is the distance between two pinned ends, $A^{CW}$ and $A^{CCW}$ are the areas of adjacent clockwise and counter-clockwise twisting domains, respectively (*i.e.*, adjacent to the free disclination). $\beta$ is half of the angle spanned by the bent disclination line.

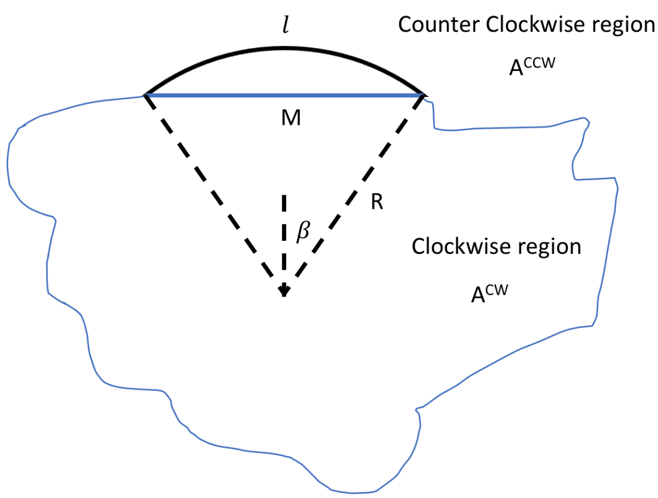


Figure S2: Schematic plot of the bending disclination in the magnetic field. The sizes are not to scale.

## 2.1 Geometry

The following relations are obtained from geometry

$$\beta = \arcsin\left(\frac{M}{2R}\right). \tag{S.3}$$

$$l = 2\beta R = 2R \arcsin\left(\frac{M}{2R}\right). \tag{S.4}$$

$$
\begin{aligned}
A^{CCW} &= \beta R^2 - \frac{M}{2}\sqrt{R^2 - \frac{M^2}{4}} \\
&= R^2 \arcsin\left(\frac{M}{2R}\right) - \frac{M}{2}\sqrt{R^2 - \frac{M^2}{4}}.
\end{aligned} \tag{S.5}
$$

Differentiation with respect to $R$ gives

$$
dl = [2\arcsin\left(\frac{M}{2R}\right) - \frac{M}{R}\frac{1}{\sqrt{1-\frac{M^2}{4R^2}}}]dR. \tag{S.6}
$$

$$
dA^{CW} = [2R\arcsin\left(\frac{M}{2R}\right) - \frac{M}{\sqrt{1-\frac{M^2}{4R^2}}}]dR = Rdl. \tag{S.7}
$$

By the conservation of area:

$$
dA^{CCW} = -dA^{CW}. \tag{S.8}
$$

## 2.2 Energy balance

Optimization of the free energy Eq. (6) of the main text with respect to perturbation of $l$ yields

$$
\begin{aligned}
dF &= f_t^{CCW} L dA^{CCW} + f_t^{CW} L dA^{CW} + f_H^{CCW} L dA^{CCW} + f_H^{CW} L dA^{CW} + f_l dl \\
&= (f_t^{CW} - f_t^{CCW}) L dA^{CW} + (f_H^{CW} - f_H^{CCW}) L dA^{CW} + f_l dl \\
&= (f_t^{CW} - f_t^{CCW}) L R dl + (f_H^{CW} - f_H^{CCW}) L R dl + f_l dl
\end{aligned} \tag{S.9}
$$

Equilibrium condition of $dF = 0$ yields

$$
(f_t^{CW} - f_t^{CCW} + f_H^{CW} - f_H^{CCW}) L R + f_l = 0 \tag{S.10}
$$

## 2.3 Twisting and magnetic energy

The director $\hat{\mathbf{n}}$ lies parallel to the substrate. Let $\hat{\mathbf{n}} = (\cos\phi, \sin\phi, 0)$, where $\phi$ varies from 0 to $\pi/2 + \theta$ in the CW regions and from 0 to $-\pi/2 + \theta$ in the

CCW regions. As described in the main text, $\theta$ is the misalignment angle for the rubbing directions being perpendicular to each other. $\hat{\mathbf{n}}$ has a uniform twist in the vertical direction ($\hat{\mathbf{z}}$) perpendicular to the substrate when it is away from the disclination. Magnetic field is $\mathbf{B} = B(\cos\frac{\pi}{4}, \sin\frac{\pi}{4}, 0)$.
The average twisting energy integrated over sample thickness is

$$f_t^{CW} = \frac{1}{2}K_{22}(\frac{\pi/2+\theta}{L})^2. \tag{S.11}$$

$$f_t^{CCW} = \frac{1}{2}K_{22}(\frac{\pi/2-\theta}{L})^2. \tag{S.12}$$

Thus,

$$f_t^{CW} - f_t^{CCW} = K_{22}\frac{\pi\theta}{L^2}. \tag{S.13}$$

The average magnetic energy integrated over sample thickness is

$$\begin{aligned} f_H^{CW} &= -\frac{1}{2}\Delta\chi\frac{1}{\mu_0}\frac{1}{L}\int_0^L[(\hat{\mathbf{n}}\cdot\mathbf{B})^2 - B^2]dz \\ &= -\frac{\Delta\chi B^2}{2\mu_0 L}[-L + \int_0^L \cos^2(\phi - \pi/4)dz] \\ &= -\frac{\Delta\chi B^2}{2\mu_0 L}[-L + \frac{L}{\pi/2+\theta}\int_0^{(\pi/2+\theta)}\cos^2(\phi-\pi/4)d\phi] \\ &= -\frac{\Delta\chi B^2}{2\mu_0}[-\frac{1}{2} + \frac{1}{2}\frac{\cos(2\theta)+1}{\pi+2\theta}]. \end{aligned} \tag{S.14}$$

Similarly,

$$f_H^{CCW} = -\frac{\Delta\chi B^2}{2\mu_0}[-\frac{1}{2} + \frac{1}{2}\frac{\cos(2\theta)+1}{-\pi+2\theta}]. \tag{S.15}$$

Thus,

$$f_H^{CW} - f_H^{CCW} = -\frac{\Delta\chi B^2}{2\mu_0}\frac{\pi[\cos(2\theta)+1]}{\pi^2 - 4\theta^2}. \tag{S.16}$$

## 2.4 Relation between curvature and the magnetic field

We next plug in the twisting and magnetic energy terms into the equilibrium condition and rearrange to obtain:

$$
\begin{aligned}
\frac{1}{R} &= -\frac{L}{f_l}(f_t^{CW} - f_t^{CCW} + f_H^{CW} - f_H^{CCW}) \\
&= \frac{L}{f_l}\{-K_{22}\frac{\pi\theta}{L^2} + \frac{\Delta\chi B^2}{2\mu_0}\frac{\pi[\cos(2\theta)+1]}{\pi^2 - 4\theta^2}\}.
\end{aligned} \tag{S.17}
$$

This is Eq. (7) of the main text.

# 3 Additional results of disclinations in the magnetic field

## 3.1 Video of a bending disclination in the magnetic field

A video file showing how the disclinations bend and eventually disappear under an increasing magnetic field is included as a separate ESI file (15p9um.avi). The sample cell thickness is 15.9 $\mu$m.

## 3.2 Curvature of other bending disclinations in the magnetic field

Figures S3 (a-d) show the bending curvature of disclinations as a function of magnetic field strength for samples with thickness 5.9, 7.2, 15.9, and 27.3 $\mu$m, respectively.

## 3.3 Misalignment angle $\theta$

Figure S4 shows the deviation of the difference in anchoring directions as a function of cell thickness from fitting the relation of bending curvature of the disclination and the magnetic field strength to Eq. (7) of the main text.

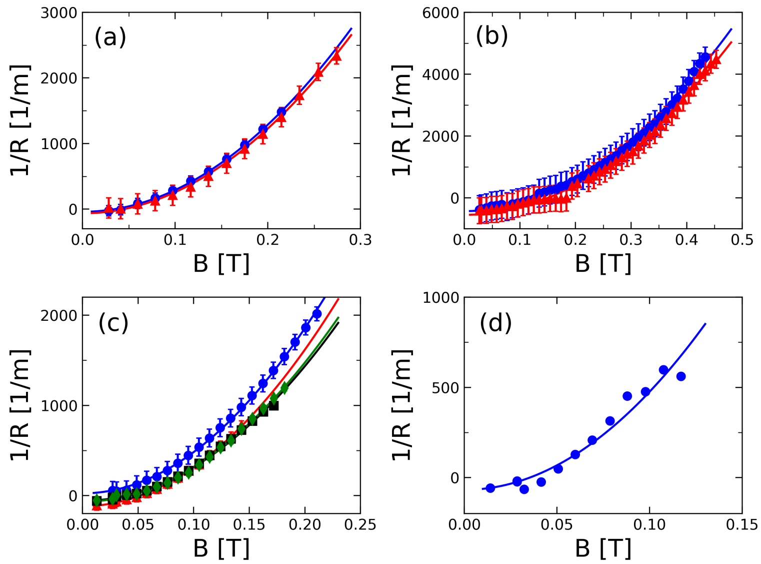


Figure S3: Curvature of bending disclination as a function of the magnetic field strength. Solids lines are best fits using Eq. (S.17). Sample thickness $L$ is (a)5.9, (b)7.2, (c)15.9, and (d)27.3 $\mu$m.

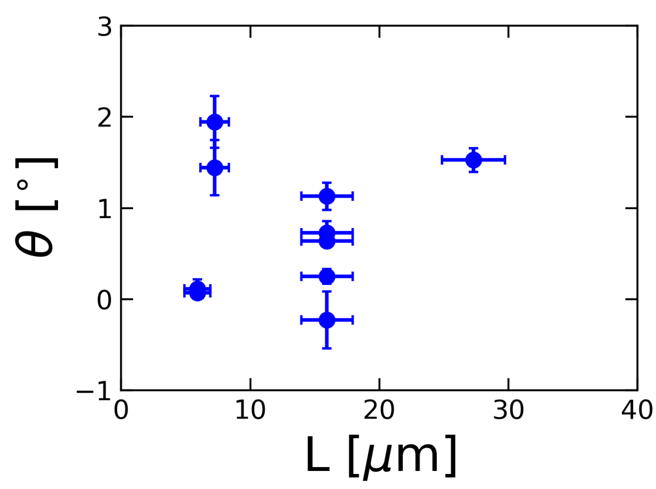


Figure S4: Deviation of the difference in anchoring directions as a function of cell thickness.

# 4 Simulation Results

We use the Q-tensor based Landau-de-Gennes (LdG) numerical model which simulates the relaxation of a nematic liquid crystal in a twist cell confinement. Using a finite difference scheme, the free energy is minimized with a conjugate gradient algorithm from the ALGLIB library for C++ [1, 2].

.

While the LdG model can be used for the general case of a biaxial LC, in our simulation, we can simplify the Q tensor to the uniaxial limit. The phase (LdG) free energy is then written in terms of the tensor:

$$Q_{ij} = \frac{3}{2}S(n_i n_j - \frac{1}{3}\delta_{ij}), \tag{S.18}$$

where $n_i$ is the $i$th component of the nematic director, $\delta_{ij}$ is the Kronecker delta, and $S$ is the nematic order parameter. The nematic director can be extracted from $Q$ as the eigenvector corresponding to the largest eigenvalue, $S$. The total free energy density is a sum of the background phase free energy density and the elastic free energy density

$$f_{\text{total}} = f_{\text{phase}} + f_{\text{elastic}}. \tag{S.19}$$

The phase free energy density is defined as:

$$f_{\text{phase}} = \frac{A}{2}Tr(Q^2) + \frac{B}{2}Tr(Q^3) + \frac{C}{4}[Tr(Q^2)]^2, \tag{S.20}$$

where $Tr$ is the trace. The LdG parameters for 5CB are A = -0.172 $\times$ $10^6$ J/m$^3$, B = -2.12 $\times$ $10^6$ J/m$^3$, C = -1.73 $\times$ $10^6$ J/m$^3$. These parameters correspond to an order parameter $S_0 = 0.53$, which minimizes the phase free energy. This order parameter is consistent with experimentally measured data for 5CB at room temperature [3, 4]. The elastic free energy density is :

$$f_{\text{elastic}} = \frac{L_1}{2}\frac{\partial Q_{ij}}{\partial x_k}\frac{\partial Q_{ij}}{\partial x_k} + \frac{L_2}{2}\frac{\partial Q_{ij}}{\partial x_j}\frac{\partial Q_{ik}}{\partial x_k} + \frac{L_3}{2}Q_{ij}\frac{\partial Q_{kl}}{\partial x_i}\frac{\partial Q_{kl}}{\partial x_j}. \tag{S.21}$$

The simulation allows the order parameter to decrease in the vicinity of the disclination to minimize the total free energy. A "core" can be defined in the simulation as the region surrounding the disclination where the order parameter is lower than $S_0$. For example, if the"core" is the region in which the order parameter falls below $0.9S_0$, then such a "core" has a diameter of about L/10 in our simulations.

We can then equate the elastic free energy density in the uniaxial LdG theory to the Frank-Oseen energy density equation:

$$f_{\text{Frank}} = \frac{K_{11}}{2}(\nabla \cdot n)^2 + \frac{K_{22}}{2}[n \cdot (\nabla \times n)]^2 + \frac{K_{33}}{2}|n \times (\nabla \times n)|^2, \qquad \text{(S.22)}$$

where $K$s are the Frank elastic constants. We used $K_{11} = 5.9$ pN, $K_{22} = 4.5$ pN, $K_{33} = 9.9$ pN.

We simulate a twist cell of size 80x40x40 units (40x40x40 units for each twist domain) with a mesh size of $\Delta x = 5$ nm. For the case of infinite anchoring strength we set the top and bottom surfaces with infinite planar anchoring oriented perpendicular to each other. The simulation size is much smaller than the experiment, but because the anchoring is infinite, the result is scale free except for the defect in the center. In our simulation the disinclination core size using the criterion $S < 0.9S_0$ is much larger than in the experiment.

In order to better understand our experimental findings, we simulated NLCs in twist cell confinement in order to examine the 3D director field between two twist regions of opposite twist handedness.

The boundary conditions of the simulation consist of two flat surfaces with planar anchoring and a 90° difference between the two. In order to create two different twist regions, we start with an initial configuration of the director twisting between the two surfaces, half twisting with one handedness and the other half twisting with the other handedness, and then we let the nematic LC relax. This is shown in Fig. S5.

When we let the nematic LC relax, we find that a straight disclination forms in the center between the two surfaces; the straight disclination runs along the boundary line between the two twist regions. The director above and below the disclination adjusts so that there is a smooth 180° twist (about an axis perpendicular to the disclination) as you travel 360° around the disclination (about the axis of the disclination). A "slice" of the simulation in the $x$-$z$ plane is shown in Figure 4 of the paper, wherein we plot the component of the nematic director in this plane.

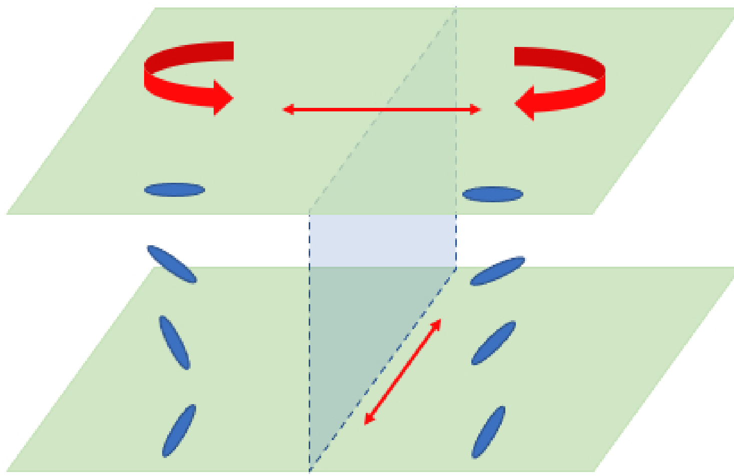

Figure S5: Initial configuration before the nematic LC is allowed to relax. Blue ovals indicate the twisted nematic director field, straight red arrows on the top and bottom indicate the anchoring orientations, twist arrows indicate the handedness of twist, and the blue plane marks the boundary between the regions of opposite handedness.

Using the simulation we can also create disclinations that do not align with one of the two substrate alignment directions. By changing the initial conditions of the simulation so that the substrates are at an angle to the plane separating regions of opposite twist handedness (while still being perpendicular to each other), the disclination again forms in the plane separating regions of opposite twist handedness.

In Figure S6, the disclination is fixed and the rubbing directions vary. It is clear that as the angle between the disclination and the bottom rubbing direction increases, the entire director field rotates about an axis parallel to the disclination. The contour levels shown in Figures S6(b-f)(bottom) at different angles basically fall on top of each other. As pointed out in the paper, all free energy considerations are independent of the orientation of the disclination. This explains why the free disclinations appear the same in the microscope regardless of their orientation relative to the rubbing directions.

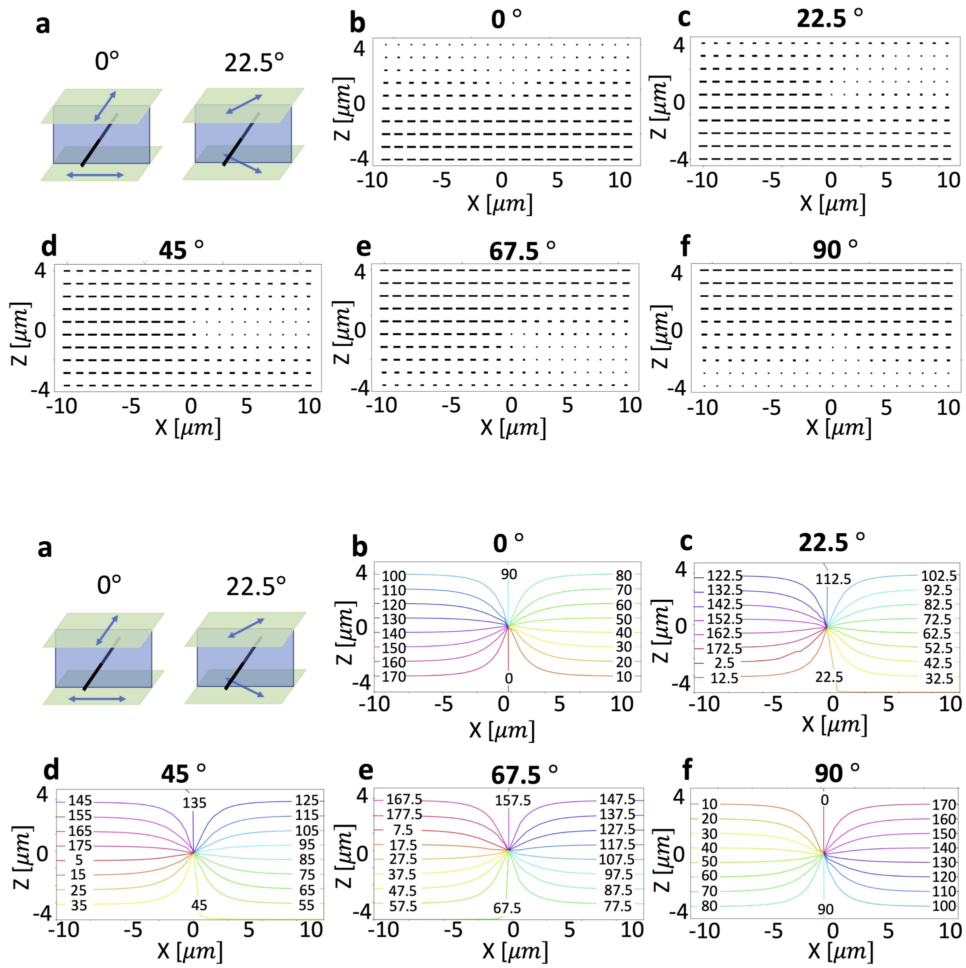


Figure S6: Simulation of the director configuration for disclinations oriented at various angles to the rubbing directions. (a) Schematic diagrams of the disclination at 0° and 22.5° with the bottom rubbing direction. The blue plane is perpendicular to the disclination. (b-f) (top) Projection of the director configuration on a plane perpendicular to the disclination (blue plane in (a)) for various angles. (b-f) (bottom) Contour levels of the angle between the director and the blue plane shown in (a) for various angles.

# 5 Bright Field Images

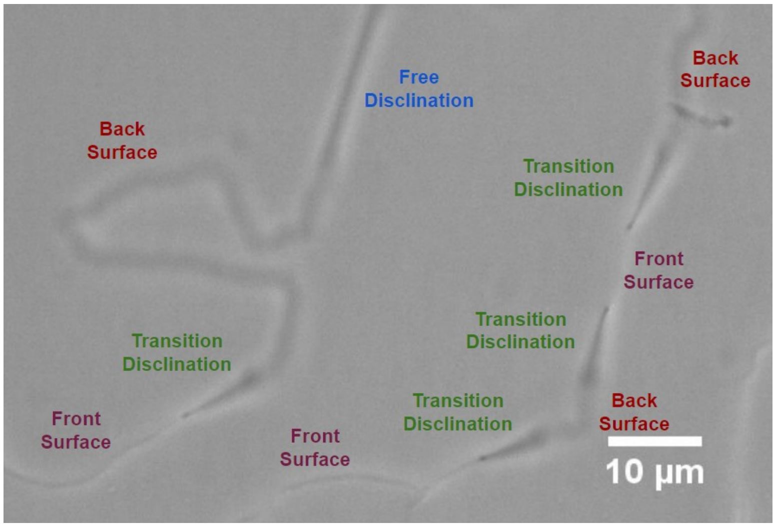


Figure S7: Bright field image of the twist disclinations. Some disclinations are on the front surface (coverslip), some are on the back surface (microscope slide), and some are in the bulk of the LC (free).

In Figure S7, the front surface disclinations are in focus, so short, free transition disclinations are visible when the disclination jumps between the two glass surfaces. As the depth of focus moves deeper into the sample, the location where the transition disclinations appear sharp moves from their front surface pinned end to the back surface pinned end. When the depth of focus reaches the back substrate, the back surface disclinations appear sharp.

# 6 POM Images

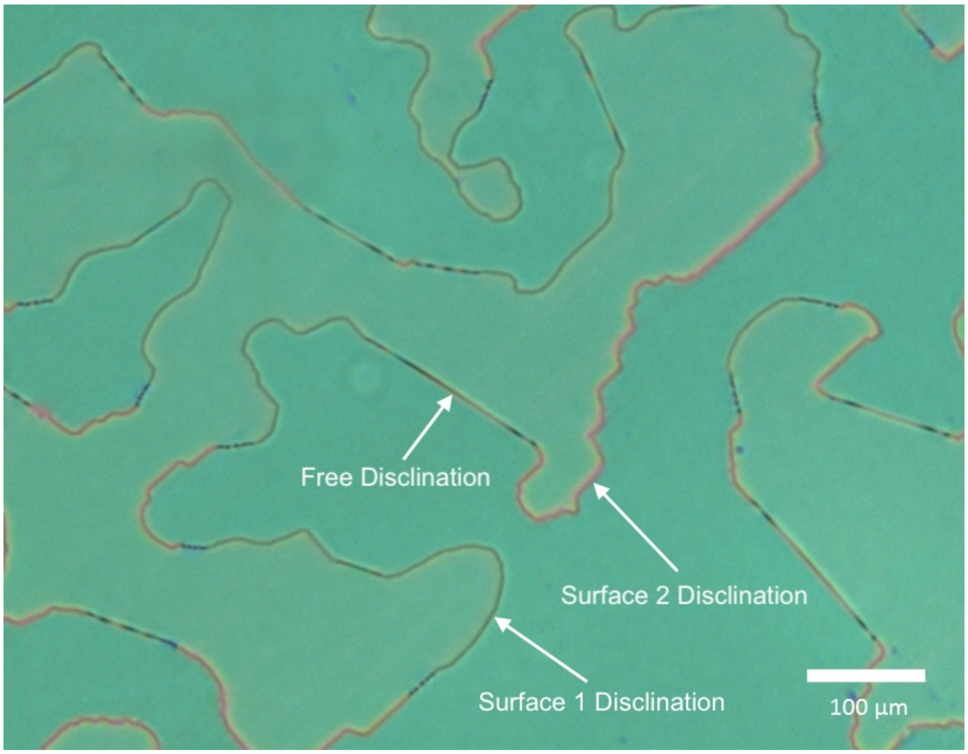


Figure S8: Polarized optical microscopy image of disclinations on the two glass substrates and free disclinations.

The two types of twist domains and the three types of disclinations can display different colors using POM depending on the orientation of the polarizers, the orientation of the sample, and the addition of a waveplate. In Figure S8, the polarizers are perpendicular to each other with the sample rotated to display the different disclination colors. No waveplate is added.

# 7 Epifluorescence Images

A video displaying a Z-scan of an 8.64 $\mu$m thick sample in epifluorescence mode is included as a separate ESI file (z-scan-epifluor.mp4). Initially the disclinations on the top surface are in focus. As the Z-scan progresses, these surface disclinations go out of focus and the free disclinations come into focus, starting at their ends and moving toward their midpoints. The $x$-$y$ scale of the image is 135 by 113 $\mu$m and Z-slices are separated by 0.27 $\mu$m.

Cross-section profiles of surface and free disclinations can be obtained using appropriate Z-slices from the video.

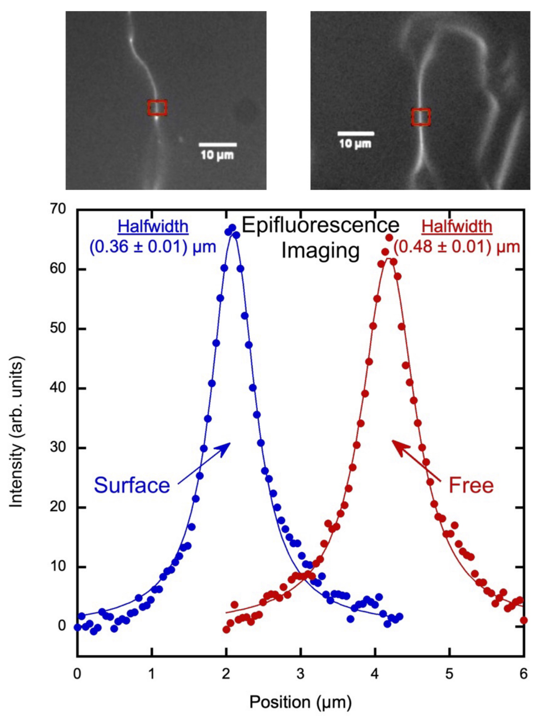


Figure S9: Cross-section profiles for a near surface (left) and free (right) disclination using epifluorescence. The data below each image are the intensity as a function of horizontal position averaged vertically within the red rectangle. The halfwidths of Lorentzian functions fit to the data are also given.

# 8 Confocal Images

The images below show three locations for the twist disclinations, running along one of the two substrates (surface disclinations) or running through the bulk of the liquid crystal (free disclinations).

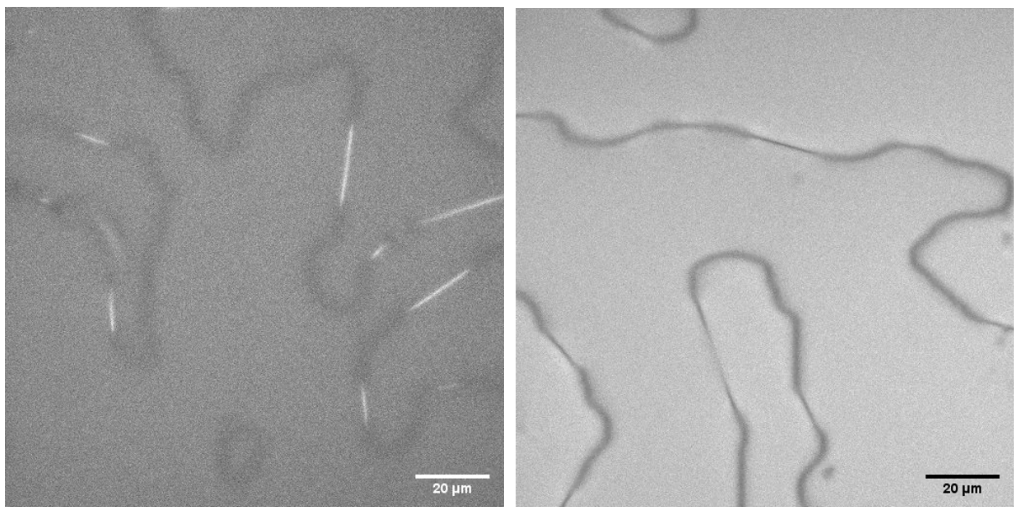


Figure S10: Free disclinations appear in focus and straight for one slice of a Z-scan using confocal microscopy. Left: Free disclinations appear bright due to laser polarization and sample orientation. Surface disclinations on the bottom substrate appear dark. Right: Free disclinations appear dark due to laser polarization and a different sample orientation. Surface disclinations on the top substrate also appear dark.

Analysis of the images is done using ImageJ. Any point along a disclination can be brought into focus by choosing the proper Z-slice, producing an image of the disclination in the $x$-$y$ plane as shown in Fig. S10. Alternatively, rotation of all the Z-slices about the $z$-axis followed by an orthogonal view produces an image of the disclination in the $z$-$\xi$ plane (shown in Figs. 3(a) and (b) of the main text).

The width of a disclination in the $x$-$y$ plane is measured by choosing the Z-slice that brings the disclination into focus, and acquiring the intensity profile across the disclination (averaging over a few pixels parallel to the disclination). See Fig. S11. A Lorentzian function is fit to the data and the halfwidth is used as a measure of the extent of the disclination.

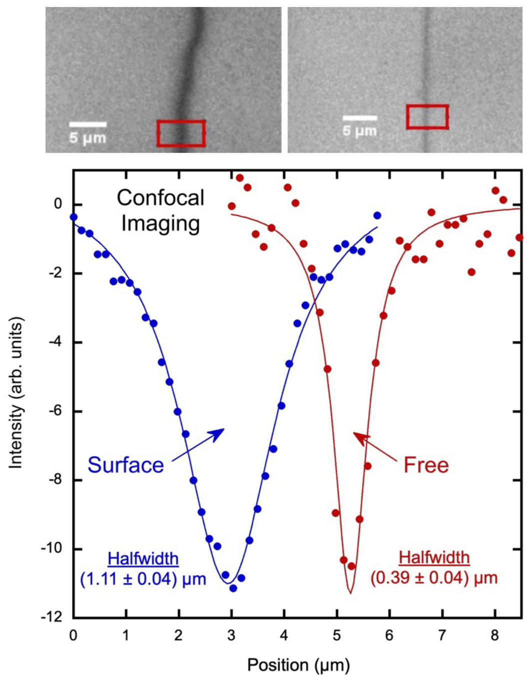


Figure S11: Cross-section profiles for a surface (left) and free (right) disclination. The data below each image are the intensity as a function of horizontal position averaged vertically within the red rectangle. The halfwidths of Lorentzian functions fit to the data are also given.

The location of the disclination along the $z$-axis is measured using the $z$-axis profile feature of ImageJ. First a small box, two or three pixels on a side, is placed near the disclination. Its $z$-axis profile shows the sharp increase and decrease in emission intensity at the coverslip and microscope slide surfaces, respectively, and a slowly decreasing intensity in between. This serves as the background profile and is shown in Fig. S12. The midpoints of the sharp increase and decrease are used as the locations of the surfaces, a method that is verified by setting the microscope to detect reflected light from the two surfaces during a Z-scan. Second, the small box is moved to the disclination and a $z$-axis profile generated. This serves as the disclination profile and is also shown in Fig. S12. The background $z$-axis profile is subtracted from the disclination $z$-axis profile, revealing a peak or valley depending on the orientation of the sample in the microscope (see Fig. S12). A Gaussian function is fit to the peak or valley, and the center position and uncertainty are used as the position along the $z$-axis (and its uncertainty) of the disclination at the chosen point in the $x$-$y$ plane. Data acquired in this manner are displayed in Figs. 3(c)-(e) of the main text.

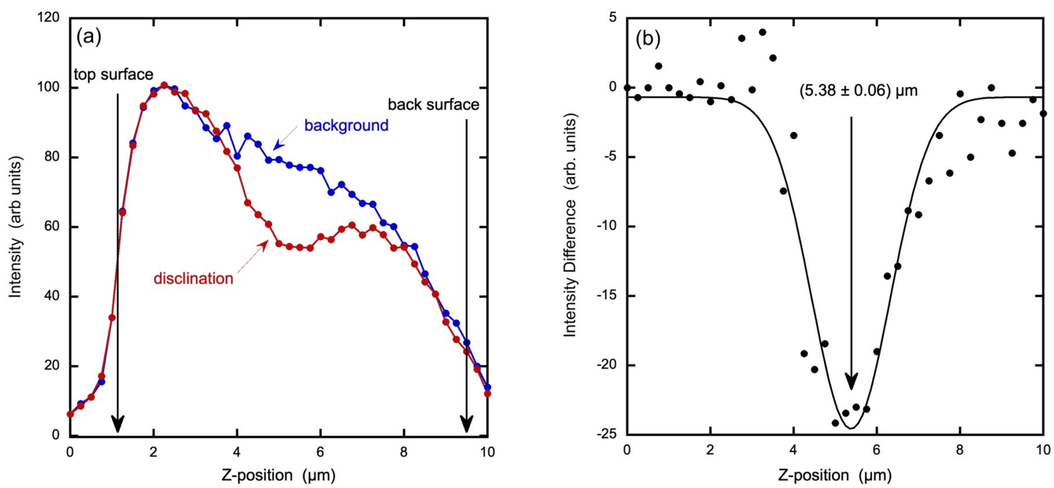


Figure S12: Determination of the z-position in the middle of the $M = 42.1$ $\mu$m free disclination in Fig. 3 of the article. The Z-profile for a point in the $x$-$y$ plane just "off" the disclination (background) and "on" the disclination (disclination) are shown in (a), along with the location of the top and bottom surfaces. The difference between the disclination and background profiles is shown in (b), along with a Gaussian fit.

# References


[1] D. M. Sussman and D. A. Beller, “Fast, scalable, and interactive software for landau-de gennes numerical modeling of nematic topological defects,” *Frontiers in Physics*, vol. 7, p. 204, 2019.

[2] “Alglib - numerical analysis library.” [Online]. Available: www.alglib.net

[3] M. Ravnik and S. Žumer, “Landau–de gennes modelling of nematic liquid crystal colloids,” *Liquid Crystals*, vol. 36, no. 10-11, pp. 1201–1214, 2009.

[4] A. Sanchez-Castillo, M. A. Osipov, and F. Giesselmann, “Orientational order parameters in liquid crystals: a comparative study of x-ray diffraction and polarized raman spectroscopy results,” *Physical Review E—Statistical, Nonlinear, and Soft Matter Physics*, vol. 81, no. 2, p. 021707, 2010.